Bragg Reflection and Conversion Between Helical Bloch Modes in Chiral Three-Core Photonic Crystal Fiber

Sébastien Loranger, Yang Chen, Paul Roth, Michael H. Frosz, Gordon K. L. Wong, and Philip St. J. Russell

***Abstract*—Optical fiber modes carrying orbital angular momentum (OAM) have many applications, for example in mode-division-multiplexing for optical communications. The natural guided modes of *N*-fold rotationally symmetric optical fibers, such as most photonic crystal fibers, are helical Bloch modes (HBMs). HBMs consist of a superposition of azimuthal harmonics (order *m*) of order $\ell_{\mathrm{A}}^{(m)} = \ell_{\mathrm{A}}^{(0)} + mN$. When such fibers are twisted, these modes become circularly and azimuthally birefringent, that is to say HBMs with equal and opposite values of $\ell_{\mathrm{A}}^{(0)}$ and spin *s* are non-degenerate. In this article we report the use of Bragg mirrors to reflect and convert HBMs in a twisted three-core photonic crystal fiber, and show that by writing a tilted fiber Bragg grating (FBG), reflection between HBMs of different orders becomes possible, with high wavelength-selectivity. We measure the near-field phase and amplitude distribution of the reflected HBMs interferometrically, and demonstrate good agreement with theory. This new type of FBG has potential applications in fiber lasers, sensing, quantum optics, and in any situation where creation, conversion, and reflection of OAM-carrying modes is required.**

***Index Terms*—Fiber bragg gratings, helical bloch modes, orbital angular momentum, twisted fiber.**

I. Introduction

LAGUERRE or Hermite Gaussian beams with different orders of orbital angular momentum (OAM) can be superimposed and used as orthogonal channels for transmitting quantum and classical information [1]. This has been explored both in free-space [2] and in optical fibers with circularly symmetric cylindrical or annular cores [3]. In recent years it has been shown that optical fibers with N-fold rotationally symmetric structures (such as most photonic crystal fibers - PCFs) support helical Bloch modes (HBMs) that consist of superpositions of Bessel beams with azimuthal order $\ell_{\mathrm{A}}{}^{(\mathrm{m})} = \ell_{\mathrm{A}}{}^{(0)} + mN$ where *m* is an integer [4]. These may be viewed as HBM harmonics that are coupled together by Bragg scattering in the azimuthally periodic fiber structure. When such a PCF is produced with a permanent helical twist (for example by spinning the preform during the draw), translational symmetry is broken and left- and right-handed versions of the same HBM become non-degenerate. Twisted PCFs are also circularly birefringent [5], making them of interest in Faraday-effect current sensing when preservation of circular polarization state is highly desirable [6]. They can also provide strong circular dichroism [4], allow generation of broad-band circularly polarized supercontinuum light [7] and even permit guidance of light in the absence of any structural core [8], [9].

Although OAM modes can be readily synthesized and interconverted in free space, this is not so easy to achieve directly in fiber, useful though this would be in many applications, such as mode-division-multiplexing in telecommunications [2], [3].

Here we report that a fiber Bragg grating (FBG), inscribed at a small angle to the fiber axis, permits narrow-band reflection and interconversion of OAM-carrying HBMs in a twisted three-core PCF (preliminary results were presented in [10]). There have been previous reports of FBGs written into twisted single-mode fiber (SMF) [11], [12], when the accidental non-centricity of the core causes the FBG to be sampled periodically — a superlattice effect that is related to the results reported here, although SMF does not support OAM-carrying HBMs. Untilted FBGs written in untwisted multi-mode fibers can reflect OAM [13], although the lack of chirality means that it is not possible to distinguish between modes with equal and opposite OAM order. We report here that a tilted FBG written into three-core twisted PCF permits wavelength-selective interconversion between HBMs of arbitrary order.

II. Theory

In this section we describe the characteristics of the backward and forward HBMs in a twisted three-fold rotationally symmetric fiber consisting of three cores arranged symmetrically around the axis (Fig. 1a) and analyze their reflection at a slanted FBG. This new model clarifies the preliminary results in [10], where the origins of the observed reflection peaks were not yet well understood.

Manuscript received January 8, 2020; revised February 18, 2020 and March 24, 2020; accepted March 26, 2020. Date of publication April 2, 2020; date of current version July 23, 2020. This work was supported by the Max-Planck-Gesellschaft (MPG). *(Corresponding author: Sébastien Loranger.)*

Sébastien Loranger, Yang Chen, Paul Roth, Michael H. Frosz, and Gordon K. L. Wong are with the Max Planck Institute for the Science of Light, 91058 Erlangen, Germany (e-mail: sebastien.loranger@mpl.mpg.de; yang.chen@mpl.mpg.de; paul.roth@mpl.mpg.de; michael.frosz@mpl.mpg.de; gordon.wong@mpl.mpg.de).

Philip St. J. Russell is with the Max Planck Institute for the Science of Light, 91058 Erlangen, Germany, and also with Department of Physics, Friedrich-Alexander-Universität, 91058 Erlangen, Germany (e-mail: philip.russell@mpl.mpg.de).

Color versions of one or more of the figures in this article are available online at http://ieeexplore.ieee.org.

Digital Object Identifier 10.1109/JLT.2020.2984464

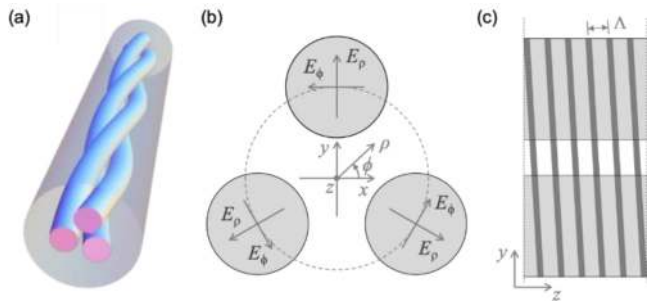

Fig. 1. (a) 3D sketch of the twisted 3-core PCF. (b) Cylindrical coordinate system used in the theory, depicting the radial and azimuthal components of the electric field in each core. (c) Side-view of the core structure (in gray) with the grating planes (slanted at a small angle γ) marked in.

A. The HBMs

It is known that the HBMs in N-fold symmetric twisted PCFs are almost perfectly circularly polarized [4], which permits us to write the monochromatic field phasors of forward (+) and backward (−) HBMs in the general form:

$$\mathbf{E}_+(\rho,\phi,z) = \frac{(1,+is_+)}{\sqrt{2}} a_+(\rho,\phi-\alpha z)\exp\left(i\beta_+ z + i\ell_{\mathrm{A}+}^{(0)}\phi\right)$$

$$\mathbf{E}_-(\rho,\phi,z) = \frac{(1,-is_-)}{\sqrt{2}} a_-(\rho,\phi-\alpha z)\exp\left(-i\beta_+ z - i\ell_{\mathrm{A}+}^{(0)}\phi\right) \quad (1)$$

with $\mathbf{E}_\pm = (e_\rho, e_\phi)_\pm$ expressed in cylindrical (ρ, ϕ) components, where α is the twist rate in rad/m, $s_i = \pm 1$ the spin and the time variation $\mathrm{e}^{-i\omega t}$ is assumed. Note that the expressions in (1) satisfy the requirement that E_+ and E_- for the same mode (i.e., $s_+ = s_-$ and $\ell_{\mathrm{A}+}{}^{(0)} = \ell_{\mathrm{A}-}{}^{(0)}$) are complex conjugates. The transverse field profile a_i (for the i-th HBM, whether forward (+) or backward (−)) is azimuthally periodic, following the twist of the fiber and sharing its N-fold symmetry at all points along the axis. It can be expressed as a Fourier series:

$$a_i(\rho,\phi-\alpha z) = a_i(\rho,\phi-\alpha z+2\pi/N) = \sum_m a_i^{(m)}(\rho)\mathrm{e}^{imN(\phi-\alpha z)}. \quad (2)$$

The integer $\ell_{\mathrm{A}i}^{(0)}$ is the azimuthal order of the $m = 0$ harmonic of the i-th HBM, or the number of complete periods of phase progression around the azimuth, for transverse field components evaluated in cylindrical coordinates (ρ, ϕ), as sketched in Fig. 1(b). Equations (1) and (2) show that the m-th harmonic in the Fourier series has azimuthal order $\ell_{\mathrm{A}i}^{(m)} = \ell_{\mathrm{A}i}^{(0)} + mN$.

The propagation constant β_i of the $m = 0$ harmonic of the i-th HBM can be expressed, to a good approximation, in the analytical form [4]:

$$\beta(\ell_{\mathrm{A}i}^{(0)}) = \beta_i = \beta_0\sqrt{1+\alpha^2\rho^2} - \alpha\ell_{\mathrm{A}i}^{(0)} + 2\kappa_{\mathrm{C}}\cos\left(\frac{2\pi}{N}(\ell_{\mathrm{A}i}^{(0)} - s_i - \beta_0\alpha\rho^2)\right) \quad (3)$$

where κ_{C} is the coupling constant between neighboring cores, $\beta_0 = 2\pi n_0/\lambda$ is the propagation constant and n_0 the effective index of the mode in an isolated core, and λ is the wavelength. Equations (2) and (3) reveal that the m-th HBM harmonic has a discrete propagation constant given by $\beta_i + mN\alpha$. Note also that since OAM is measured in the Cartesian laboratory frame, the OAM order of the m-th harmonic is given by $\ell_{\mathrm{OAM}}^{(\mathrm{m})} = \ell_{\mathrm{A}i}^{(m)} - s_i$. This has the interesting consequence that the harmonics of two different HBMs, one with $\ell_{\mathrm{A}i}^{(0)} = q$ and $s = -1$ and the other with $\ell_{\mathrm{A}i}^{(0)} = q+2$ and $s = +1$, will share the same value of OAM.

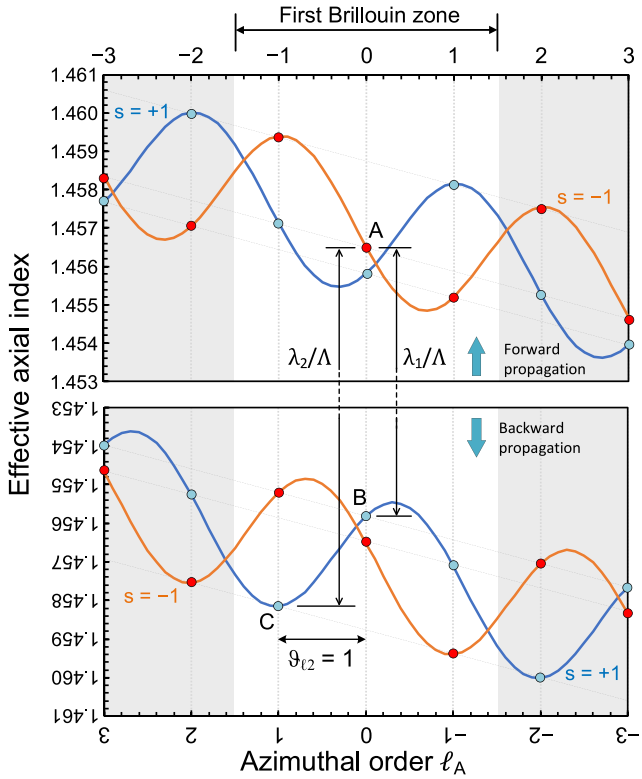

Fig. 2. Dispersion diagram of the modes in the system in the forward and backward direction from (3). The backward direction is a 180° rotation of the forward diagram (note the reversed axes). Two Bragg reflections are shown. At λ_1 conversion is between forward and backward modes with zero azimuthal order and opposite spins (scattering from A to B). At λ_2 conversion is between an $\ell_{\mathrm{A}} = 0$ forward mode and an $\ell_{\mathrm{A}} = +1$ backward mode, i.e., $\vartheta_\ell = +1$ (scattering from A to C). The sum of the backward and forward refractive indices adds up to λ_i/Λ in each case, where Λ is the grating pitch.

The HBM model can be generalized to multi-core single-ring structures [14], [15] by choosing appropriate values of κ_{c}, ρ, N and β_0. The modal refractive indices $n_\pm = \beta_\pm\lambda/2\pi$ from (3) are plotted versus azimuthal order in Fig. 2. HBMs form only at integer values of $\ell_{\mathrm{A}i}^{(0)}$ (marked by thin vertical lines and encircled points). The best fit to a series of experimentally measured Bragg peaks was found for $\kappa_{\mathrm{C}} = 3570\ \mathrm{m}^{-1}$. The radial position of the cores (estimated from an optical micrograph) was 2.5 μm, and $n_0 = 1.457$ was calculated by finite element modeling (FEM).

B. Bragg Reflection

To analyze the Bragg reflection of HBMs, we introduce slowly varying, complex-valued, scalar envelope functions V_+ and V_- for the backward and forward modes, writing the total electric

field with the Ansatz:

$$\mathbf{E}_{\rm tot} = V_+(z)\mathbf{E}_+ + V_-(z)\mathrm{e}^{i\vartheta z}\mathbf{E}_- \tag{4}$$

where $\vartheta = \beta_+ + \beta_- - K_z$ is a parameter describing detuning from the Bragg condition caused by changes in average index and wavelength, and K_z is the z-component of the grating vector$\mathbf{K} = (K_x, K_y, K_z) = (0, \sin\gamma, \cos\gamma)2\pi/\Lambda$, where γ the slant angle of the grating planes, assumed without loss of generality to be tilted about the x-axis. Introducing ϑ in this way makes the final coupled mode equations easier to understand and manipulate [16]. Substituting (4) into the wave equation, and following a standard coupled mode analysis, yields the equations:

$$\frac{\partial V_+}{\partial z} = i\kappa_+(z)V_-, \frac{\partial V_-}{\partial z} = -i\kappa_-(z)V_+ + i\vartheta V_- \tag{5}$$

where the coupling constants are given by:

$$\kappa_+(z) = \frac{\pi(1 - s_+s_-)\sqrt{1+\rho^2\alpha^2}}{4\lambda n_+}\frac{\iint_A Q(\rho,\psi)\mathrm{e}^{-i\vartheta_\ell\phi}\,dA}{\iint_A a_+^2 dA}$$

$$Q(\rho,\psi) = a_+(\rho,\psi)a_-(\rho,\psi)n_{\rm G}(\rho,\psi)\mathrm{e}^{iK\rho\sin\gamma\sin\phi} \tag{6}$$

where $\kappa_+ \simeq \kappa_-^*$, $\psi = \phi - \alpha z$, $\vartheta_\ell = \ell_{\rm A+} + \ell_{\rm A-}$ is the dephasing of the azimuthal order, $n_\pm = \beta_\pm\lambda/2\pi$ are the effective modal indices of the HBMs, and $n_{\rm G}$ is the refractive index modulation depth of the FBG, which is assumed to be non-zero only in the cores. It is calculated from the relative dielectric constant as $n = (\varepsilon_0 + \varepsilon_1\cos\mathbf{K}\cdot\mathbf{r})^{1/2}$, which approximates to $n_0 + n_{\rm G}\cos(\mathbf{K}\cdot\mathbf{r})$,

with $n_0 = \sqrt{\varepsilon_0}$ and $n_{\rm G} = \varepsilon_1/2n_0$, assuming $\varepsilon_1 << \varepsilon_0$, as is typical for FBGs. Equation (6) shows that for non-zero reflection the spin must always reverse sign. To simplify the analysis we now approximate Q in separable form as:

$$Q(\rho,\phi-\alpha z) = n_{\rm G}R(\rho)F(\phi-\alpha z)\exp(iK\rho_{\rm co}\sin\gamma\sin\phi) \tag{7}$$

where $\rho_{\rm co}$ is the radial position of the core centers and α z is the position-dependent phase offset between the grating and the twisting fiber structure. This permits the integral in the numerator in (6) to be interpreted as the angular Fourier transform of the non-sinusoidal quantity:

$$F(\phi-\alpha z)\exp(iK\rho_{\rm co}\sin\gamma\sin\phi) \tag{8}$$

yielding azimuthal harmonics. Assuming circular cores (diameter 2.7 μm, centered at $\rho_{\rm co} = 2.5$ μm) and Gaussian mode shapes in each core (full-width-half-maximum 2.4 μm, based on finite element modelling), the relative strengths of these harmonics, normalized to the values at zero tilt angle, can be calculated. They are plotted in Fig. 3 for three different tilt angles and normalized to the highest values of κ_+, which occurs when $\vartheta_\ell = 0$ and there is no tilt.

At zero grating tilt the Fourier transform of (8) is independent of αz because $F(\phi - \alpha z)$ is has exactly three periods around the azimuth, so that the coupling constant is non-zero only when ϑ_ℓ is a multiple of 3 and $F(\phi - \alpha z)$ is non-sinusoidal. For a tilted grating, however, the three-fold rotational symmetry of $F(\phi - \alpha z)$ is broken, and the coupling can in general take non-zero for all values of ϑ_ℓ. In addition, because the cores rotate axially relative to the grating, the coupling constant oscillates with z with period $2\pi/3\alpha$. This creates an optical superlattice [17], resulting in the appearance of reflection sidebands on either side of the main Bragg peak (at $\vartheta = 0$), each p-th spatial harmonic of κ_i(z) producing sidebands at $\vartheta = \pm 3p\alpha$. For a weak FBG, these sidebands are spectrally narrow and so can be viewed as independent FBGs. For strong FBGs, however, this is no longer true because the bandwidths for conversion between different modes widen and overlap spectrally, requiring a more accurate model by solving all the coupled mode equations simultaneously (see Appendix).

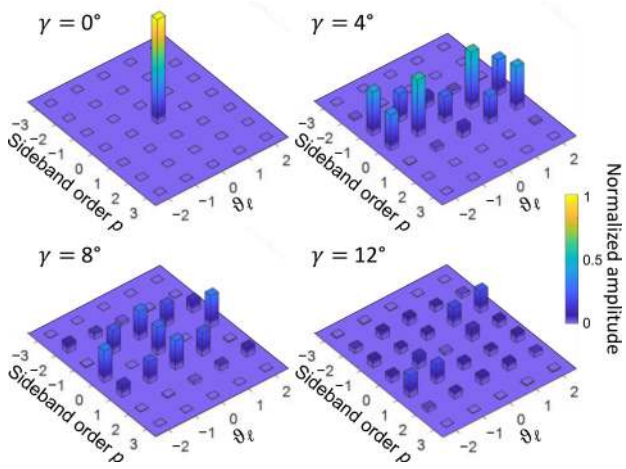

Fig. 3. Values of $|\kappa_+|$, normalized to its value at zero tilt, with increasing tilt angle, as functions of ϑ_ℓ and superlattice sideband order p.

The coupling constant for each p-th superlattice sideband can be estimated by taking the Fourier transform of $\kappa_i(z)$, and the results are plotted in Fig. 3 as functions of ϑ_ℓ and p for $\gamma = 0°$, 4°, 8° and 12° normalized to the value at zero tilt. The plot illustrates how the sidebands increase in strength and number as the tilt angle rises. The parameters used in the calculation were $\alpha = 2480$ rad/m, $\rho_{\rm co} = 2.5$ μm, $n_0 = 1.45$ (neglecting material dispersion) and $K = 2\pi/\Lambda = 2\pi/(535.3$ nm).

III. Method

A. The Optical Fiber

The three-core twisted PCF was made by stacking circular rods of silica glass into a hexagonal lattice, the three central ones, arranged in an equilateral triangle, being doped with Ge (16 mol%, yielding an NA of 0.26). The preform stack was continuously spun while the fiber was drawn, producing a built-in chiral twist. The germanosilicate glass, having a lower melting temperature than silica, flowed in between the silica rods, forming cogwheel-shaped cores, as seen in the optical micrograph in Fig. 4(a). In the drawn fiber, the diameter of the cores was 2.7 μm and their distance from the fiber axis was 2.5 μm. The individual cores are single-mode at 1550 nm with an LP_{11}-mode cut-off at 920 nm. Note that the multi-core system is multi-mode, since each individual core couples to its neighbors, thereby generating family of "super-modes" (HBMs) carrying OAM [9].

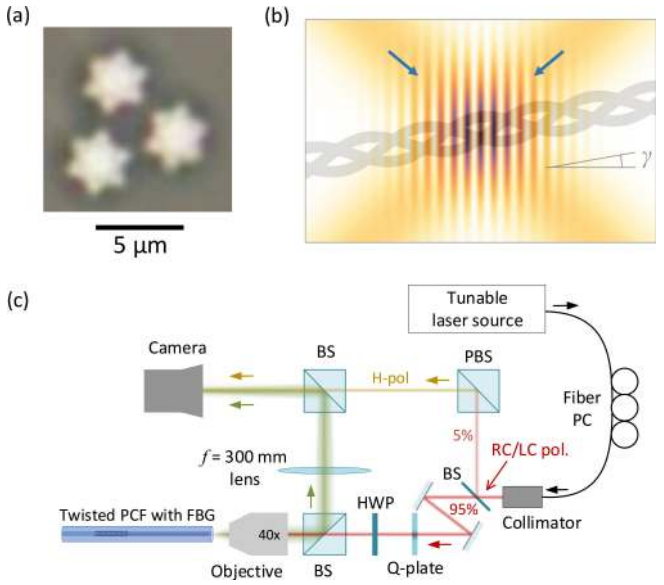

Fig. 4. (a) Optical micrograph of the end-face of the fiber used in the experiment. (b) Sketch (not to scale) of the UV interference fringes at the tilted, twisted 3-core fiber (twist rate greatly exaggerated). (c) Interferometric set-up for measuring the phase. The reflection spectrum was measured by sweeping the laser wavelength. BS: beam-splitter, PBS: polarizing beam-splitter, PC: polarization controller, HWP: half-wave plate, Q-plate: vortex wave-plate. The last two components were removable depending on the experiment.

B. FBG Writing

FBGs were written into the fiber using a Talbot interferometer (Photonova Inc.) and light from a 213 nm Q-switched laser (Xiton Photonics) [18], [19]. A sketch of the interference fringes and the twisted three-core PCF is shown in Fig. 4(b). The fiber could be tilted in the interferometer, resulting in slanted fringes, as depicted. The intrinsically high UV photosensitivity of the cores meant that FBGs could be written directly without need of H_2 loading. The system was adjusted so that, after exposure to 130 mW of UV power for between for 20 and 50 minutes, a Bragg reflection appeared at $\sim$1550 nm. We note that, although the overlap integral in (6) decreases with increased tilt, causing a drop in FBG reflectivity, this can easily be compensated for by writing a stronger FBG (we are far from saturating the photo-induced index change).

C. Measuring the Reflection Spectrum & Modes

Interferometry was used to measure the phase of the reflected mode (Fig. 4(c)). Light from a tunable laser source (wavelength resolution 1 pm) was split 5:95 at a thin-film beam-splitter. The 5% reflection was polarized horizontally and used as the reference phase, and the transmitted 95% was launched into the twisted fiber. A Q-plate was optionally placed to synthesize OAM beams [20], and a half-wave plate was available to switch the state of circular polarization. It was set to right circular (RC, $s = -1$) or left circular (LC, $s = +1$) using a fiber polarization controller. The Bragg reflection was separated out using a beam-splitter cube, and a lens with focal length 300 mm used to form a magnified image on the camera. The polarization state was monitored with a Thorlabs polarimeter, using flip mirrors placed

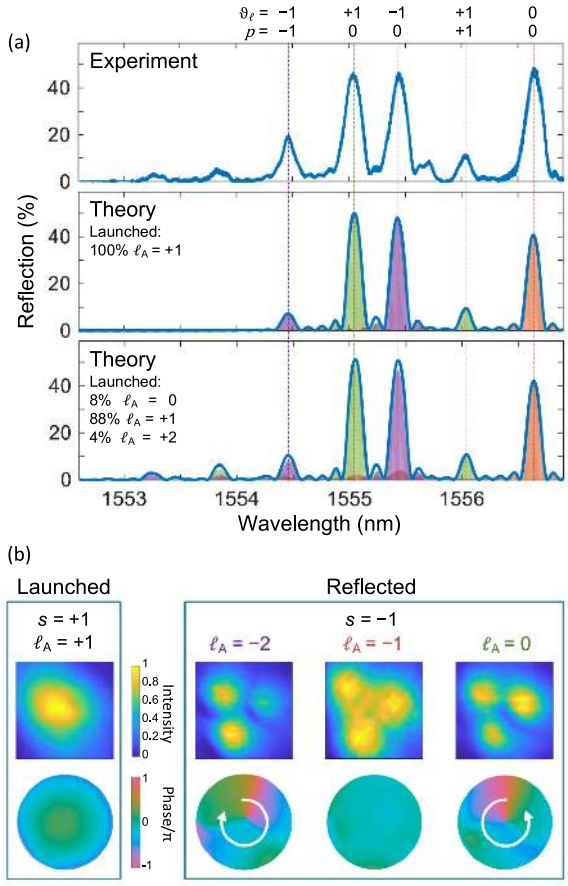

Fig. 5. (a) Upper: Reflection spectrum measured for injection of a LCP TEM_{00} mode ($\ell_{OAM} = 0$, $\ell_A = +1$, s $= +1$) into a 10-mm-long FBG written in a fiber with twist period 2.5 mm and tilt angle $\sim$3.2°. The change in azimuthal order associated with each RCP peak is marked along the top of the plot ($\vartheta_\ell = 0$ and -1). The order p of each superlattice sideband is also marked in. Middle: Reflection spectrum calculated using vector coupled multi-mode theory, assuming that only the LCP TEM_{00} mode is launched (individual modal intensities are color-coded). Lower: Calculated reflection spectrum assuming incidence of 88% of $\ell_A = +1$, 8% of $\ell_A = 0$ and 4% of $\ell_A = -1$ (all three modes in phase), showing excellent agreement with experiment. (b) Measured near-field amplitude and phase of the launched beam (left) and the three strongest reflected modes (right).

before the Q-plate and before the 300 mm lens. By introducing an angular mismatch between the reference and the image beam, interference patterns could be seen and used to retrieve the phase distribution.

Some of the Bragg reflections had quite low reflectivity, so that interference with Fresnel reflections from the cleaved fiber-end deformed the phase patterns or made them unreadable. To circumvent this problem, we used optical frequency domain reflectometry (OFDR) [21] in all the measurements of phase and amplitude.

IV. Experimental Results

In all the experiments reported here, the fibers had a twist period 2.5 mm, corresponding to $\alpha = 2513$ rad/m, which is a factor of two higher than in previously reported [10]. The higher twist rate results in more distinct reflection peaks, thus

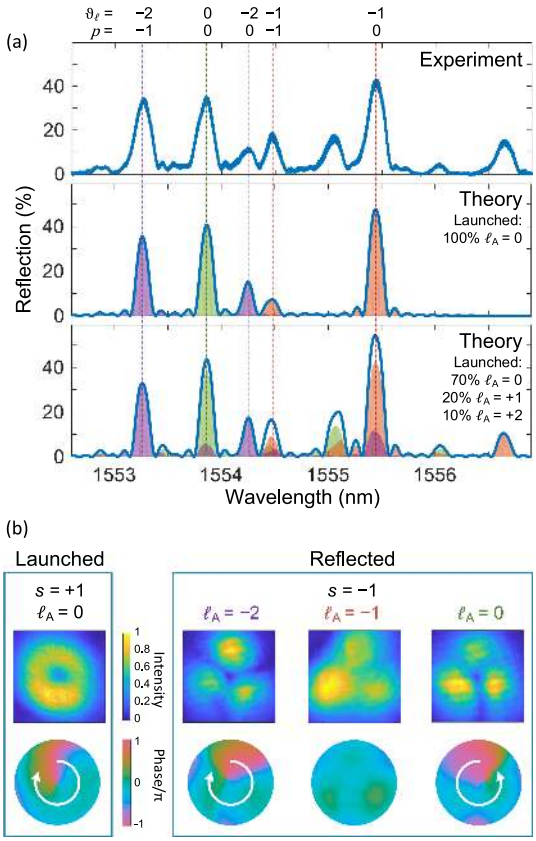

Fig. 6. (a) Upper: Reflection spectrum measured on the same FBG as in Fig. 5, for incidence of a LCP beam with $\ell_{OAM} = -1$, $\ell_A = 0$, $s = +1$. (a) The change in azimuthal order associated with each RCP peak is marked along the top of the plot ($\vartheta_\ell = 0$, -1 and -2). The order m of each superlattice sideband is also marked in. Middle: Reflection spectrum calculated using vector coupled multi-mode theory, assuming that only the LCP mode with $\ell_A = 0$ is launched (individual modal intensities are color-coded). Lower: Calculated reflection spectrum assuming incidence of 20% of $\ell_A = +1$, 70% of $\ell_A = 0$ and 10% of $\ell_A = -1$ (all three modes in phase), showing excellent agreement with experiment. (b) Measured near-field amplitude and phase of the launched beam (left) and the three strongest reflected modes (right).

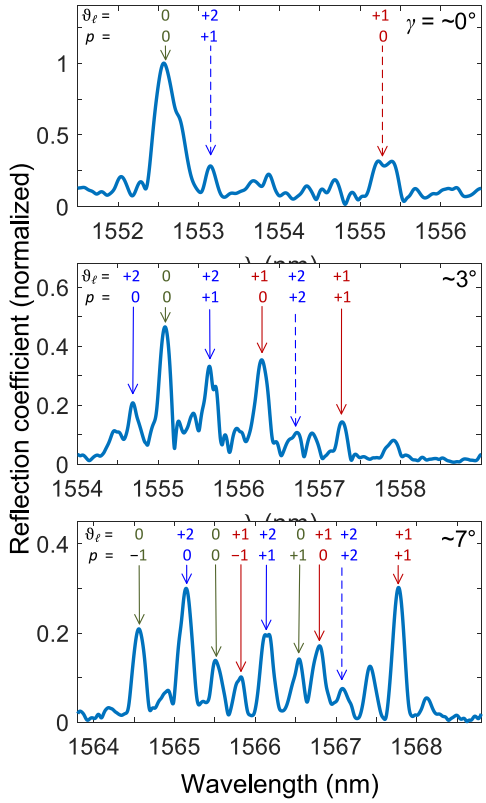

Fig. 7. Effect of increasing tilt on the reflection spectrum when a ($\ell_{OAM} = +1$, $\ell_A = 0$, $s = -1$) mode is launched into the twisted fiber. The azimuthal dephasing parameter ϑ_ℓ and the order p of the superlattice sidebands are labelled above each peak. The dashed lines indicate peaks where the signal was too low to allow the phase to be mapped (the given values of ϑ_ℓ and p are inferred from theory). In the upper plot, the additional weak peaks are caused by the tilt angle not being exactly zero. Some of the peaks are caused by accidental excitation of other modes.

allowing more precise characterization of the FBG reflections. The theoretical calculation in Figs. 5–6 comes from solving the full coupled mode theory of equations (5) (see Appendix for more details). The modulation depth of the FBGs, estimated by comparing with the theory, was $n_G = 0.0002$.

To explore the ability of slanted FBGs in multi-core twisted fibers to reflect between OAM modes of different order, a saturated FBG (50 minute exposure) was fabricated a tilt angle of ~3.2°, optimized to yield the highest reflections at $\vartheta_\ell = \pm 1$, ± 2 for an LCP TEM_{00} incident beam ($\ell_A = +1$, $s = +1$, $\ell_{OAM} = 0$) that was positioned so as to excite all three cores equally. Three main reflection peaks were observed, corresponding to $\vartheta_\ell = 0$, $\vartheta_\ell = +1$ and $\vartheta_\ell = -1$, as confirmed by the measured phase distributions in Fig. 5(b). In each case the circular polarization state was reversed, as expected. The smaller peaks correspond to superlattice side-bands of order $p = \pm 1$. They are spaced from the main Bragg peak (at λ_{B0}) by $\Delta\lambda \approx \lambda_{B0}^2 3\alpha/(4\pi n) \approx 1$ nm, where $\alpha = 2500$ rad/m and n is the average index of the backward and forward coupled modes.

In a second measurement with the same sample, a beam with $\ell_{OAM} = -1$ ($\ell_A = 0$, $s = +1$) was launched (Fig. 6). As expected, a reflected peak (green under-shaded) appears, corresponding to a backward travelling mode with the opposite chirality, i.e., $\ell_{OAM} = +1$ ($\ell_A = 0$, $s = -1$) and $\vartheta_\ell = 0$. A stronger peak (orange under-shaded, accompanied by a weak $p = -1$ superlattice sideband) appears for which $\ell_{OAM} = 0$ ($\ell_A = -1$, $s = -1$) and $\vartheta_\ell = -1$. Its wavelength exactly matches that of the $\vartheta_\ell = -1$ strong peak in Fig. 5, as expected. Two peaks (purple under-shaded) appear for which $\ell_{OAM} = -1$ ($\ell_A = -2$, $s = -1$) and $\vartheta_\ell = -2$, the stronger of them being caused by the $p = -1$ superlattice sideband, as confirmed by the overlap integrals in Fig. 3. This reflection peak has a similar origin to the side-band observed in [10] for half the twist rate. The additional peaks we attribute to contamination of the launched $\ell_{OAM} = -1$ mode by modes of different OAM order. Assuming this, we can get an excellent agreement between theory and experiment, as shown in Fig. 6(a) in the lower spectrum.

As the tilt angle increases, the periodic function $\kappa_+(z)$ becomes weaker and more anharmonic, resulting weaker Bragg peaks and more superlattice sidebands (see Fig. 3). Fig. 7 shows three spectra measured at different tilt angles for a launched mode with $\ell_A = 0$ and $s = -1$ (Fig. 6). The near-field phase

profiles at reflection were used to identify the reflected mode. At $\gamma = 0°$ there is only one strong peak, corresponding to $\vartheta_\ell = 0$ (the weak peaks are present as the tilt angle is not exactly 0° in the experiment). As γ is increased, more and more Bragg peaks appear at different values of ϑ_ℓ. Reflections at superlattice sidebands also grow in strength and number, sometimes exceeding the strength of the fundamental. At very high tilt angles, the number of Bragg peaks becomes unmanageably high, leading to overlap between different reflections and loss of selectivity. The optimal tilt angle for the three-core structure studied lay between 2° and 4°, where the reflections for $\vartheta_\ell = \pm 1$ and ± 2 were strongest.

V. Conclusion

Slanted FBGs, written in twisted fibers with *N*-fold rotationally symmetric arrangements of cores, can convert between forward and backward modes of different OAM order. This is possible because the *N*-fold symmetry is broken by the tilted Bragg planes. Although in the experiments the reflection efficiencies reached only 46%, despite long exposure times, much higher efficiencies could be obtained, if required, by hydrogen loading the fibers before exposure. The twisted FBGs provide high wavelength and OAM selectivity, due to non-degeneracy between modes with the same OAM order but opposite circular polarization state. Certain reflections are unique for a given launched mode (e.g., for $\vartheta_\ell = \pm 2$) and could potentially be used in a laser cavity to allow oscillation in a single OAM state, or in robust all-fiber OAM mode conversion/selection for mode division multiplexing. Although the transmission of doughnut-shaped OAM beams is rather low for the 3-core configuration (the overlap integral gives ~80% maximum launch efficiency), this can be optimized by improving the fiber design, for instance by increasing the number of cores. Note that the direction of spin cannot, however, be selected, since it is always reversed upon reflection.

Appendix

Here we provide details of the multi-wave coupled mode theory used to model reflections from a slanted Bragg grating in a twisted *N*-fold symmetric fiber.

A. Coupling Constant

The results of a numerical calculation of the coupling constant (using Eq. (6)), assuming Gaussian mode field profiles across each core and plotted over one period, are shown in Fig. 8. When the tilt angle γ is non-zero, the angle between the twisting three-core structure and the FBG planes oscillates, causing κ_+ to oscillate periodically along the fiber, repeating every $2\pi/3\alpha$.

A useful simplification can be made by approximating $Q(\rho, \phi - \alpha z)$ in Eq. (6) the product of functions only of ρ and ϕ:

$$Q(\rho, \phi - \alpha z) = n_{\mathrm{G}} R(\rho) F(\phi - \alpha z) \mathrm{e}^{iK\rho_{\mathrm{co}} \sin\gamma \sin\phi} \tag{9}$$

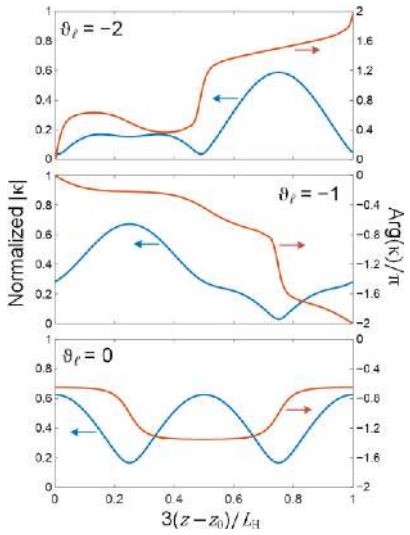

Fig. 8. Amplitude (normalized) (in blue) and phase (in red) of the coupling constant as a function of position over one period (i.e., one third of the helical pitch $L_{\mathrm{H}} = 2\pi/\alpha$) for (a) $\vartheta_\ell = -2$, (b) $\vartheta_\ell = -1$ and (c) $\vartheta_\ell = 0$ and a tilt angle of 10°, assuming Gaussian field intensity distributions (FWHM 2.3 μm) across the cores, core diameter 2.7 μm and core center to axis distance 2.5 μm. z_0 corresponds to one of the cores aligned on the positive y-axis with the tilt being in the y-z plane as shown in Fig. 1 in the manuscript.

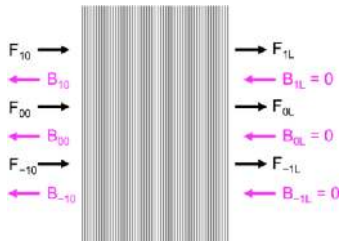

Fig. 9. Schematic representation of the fields in the multi-wave calculation.

The ratio of integrals in Eq. (6) can then be written, after canceling out the radial integrals:

$$n_{\mathrm{G}} \frac{\int_\phi F(\phi - \alpha z) \mathrm{e}^{i(K\rho_{\mathrm{co}} \sin\gamma \sin\phi - \vartheta_\ell \phi)}\, d\phi}{\int_\phi F(\phi - \alpha z) d\phi}. \tag{10}$$

If we assume that $F(\phi - \alpha z) = 1$ in each core and zero outside, and that the cores subtend an angle ϕ_{co}, this expression simplifies to:

$$n_{\mathrm{G}} \frac{\int_\phi F(\phi - \alpha z) \mathrm{e}^{i(K\rho_{\mathrm{co}} \sin\gamma \sin\phi - \vartheta_\ell \phi)}\, d\phi}{N\phi_{\mathrm{co}}} \tag{11}$$

where *N* is the number of cores and $\phi_{\mathrm{co}} < 2\pi/N$. The integral can be evaluated analytically for zero tilt, when it takes the form:

$$n_{\mathrm{G}} \frac{\mathrm{sinc}(\phi_{\mathrm{co}}\vartheta_\ell/2)}{N} \frac{\sin\pi\vartheta_\ell}{\sin(\pi\vartheta_\ell/N)} \mathrm{e}^{-i\pi\vartheta_\ell(N-1)/N} \tag{12}$$

which is in general non-zero only when ϑ_ℓ is a multiple of *N*..

B. Multi-Wave Coupled-Mode Equations

To properly model FBG reflections in the twisted fiber, multimode coupled-wave theory must be applied, including both

in-phase and out-of-phase Bragg reflections. The requirement that the circular polarization state reverses upon reflection means that only 3 modes need be considered in each direction: (ℓ_{A}, s) $= (-2, -1), (-1, -1), (0, -1)$ in the forward direction (noted as F_{-1}, F_0 and F_1 respectively) and (ℓ_{A}, s) $= (+2, +1), (+1, +1), (0, +1)$ in the backward direction (noted as B_{-1}, B_0 and B_1 respectively), or the opposite set in which the signs of all the azimuthal orders and spin are reversed.

1) Multi-Wave Bragg Scattering: When there is more than one mode propagating in each direction, they are all potentially coupled together by Bragg scattering and the analysis gets complicated. This is the case for a three-core twisted PCF with an inscribed tilted Bragg grating. Although the multiwave coupled mode equations are easy to set up, their solution requires a special procedure, as we now explain.

We first solve the coupled mode equations three times, first for $\mathrm{F}_{1\mathrm{L}} = 1$ and $\mathrm{F}_{0\mathrm{L}} = \mathrm{F}_{-1\mathrm{L}} = 0$, then for $\mathrm{F}_{1\mathrm{L}} = \mathrm{F}_{-1\mathrm{L}} = 0$ and $\mathrm{F}_{0\mathrm{L}} = 1$, and finally for $\mathrm{F}_{1\mathrm{L}} = \mathrm{F}_{0\mathrm{L}} = 0$ and $\mathrm{F}_{-1\mathrm{L}} = 1$. Each solution yields three matrix elements in the equations:

$$\begin{bmatrix} B_{10} \\ B_{00} \\ B_{\bar{1}0} \end{bmatrix} = \begin{bmatrix} m_{11} & m_{10} & m_{1\bar{1}} \\ m_{01} & m_{00} & m_{0\bar{1}} \\ m_{\bar{1}1} & m_{\bar{1}0} & m_{\bar{1}\bar{1}} \end{bmatrix} \begin{bmatrix} F_{1L} \\ F_{0L} \\ F_{\bar{1}L} \end{bmatrix} \tag{13}$$

and

$$\begin{bmatrix} F_{10} \\ F_{00} \\ F_{\bar{1}0} \end{bmatrix} = \begin{bmatrix} r_{11} & r_{10} & r_{1\bar{1}} \\ r_{01} & r_{00} & r_{0\bar{1}} \\ r_{\bar{1}1} & r_{\bar{1}0} & r_{\bar{1}\bar{1}} \end{bmatrix} \begin{bmatrix} F_{1L} \\ F_{0L} \\ F_{\bar{1}L} \end{bmatrix} \tag{14}$$

Equations (13) and (14) can be written as:

$$\mathbf{B}_0 = [\mathbf{M}] \cdot \mathbf{F}_L \quad \text{and} \quad \mathbf{F}_0 = [\mathbf{R}] \cdot \mathbf{F}_L \tag{15}$$

and manipulated to yield:

$$\mathbf{B}_0 = [\mathbf{M}][\mathbf{R}]^{-1} \cdot \mathbf{F}_0 \quad \text{and} \quad \mathbf{F}_L = [\mathbf{R}]^{-1} \cdot \mathbf{F}_0 \tag{16}$$

where $[\mathbf{M}][\mathbf{R}]^{-1}$ is the reflection matrix and $[\mathbf{R}]^{-1}$ the transmission matrix for an arbitrary input field.

2) Coupled Mode Equations: Before solving the coupled mode equations we need first to numerically integrate Eq. (6) to calculate the coupling constant for each pair of coupled modes over one period $2\pi/3\alpha$, and then find the amplitude and phase of its *p*-th spatial harmonic by expressing it as a Fourier series (reconstructing the coupling constant from its Fourier harmonics ensures that it is exactly periodic). Next the parameters describing dephasing from the Bragg condition are calculated for each interaction:

$$\vartheta_{ij} = \beta_i + \beta_j - K_z = 2\beta_0\sqrt{1+\alpha^2\rho^2} - \alpha\left(\ell_{\mathrm{A}i}^{(0)} + \ell_{\mathrm{A}j}^{(0)}\right) - K_z + 2\kappa_{\mathrm{C}} \begin{bmatrix} \cos\left(2\pi(\ell_{\mathrm{A}i}^{(0)} - s_i - \beta_0\alpha\rho^2)/N\right) \\ +\cos\left(2\pi(\ell_{\mathrm{A}j}^{(0)} + s_i - \beta_0\alpha\rho^2)/N\right) \end{bmatrix}. \tag{17}$$

We are now in a position to set up the coupled equations. An appropriate field Ansatz is:

$$\mathbf{E}_{\mathrm{tot}} = \frac{(1, +is_+)}{\sqrt{2}} \sum_{q=1,0,\bar{1}} a_q(\rho, \phi - \alpha z) \cdot \left(F_q(z)\mathrm{e}^{i(\bar{\beta}z + \ell_{\mathrm{A}q}^{(0)}\phi)} + B_q(z)\mathrm{e}^{i[(\bar{\beta}-K_z)z - \ell_{\mathrm{A}q}^{(0)}\phi]}\right) \tag{18}$$

where the z-dependent phase progression is expressed relative to a reference wavevector $\bar{\beta}$ (which can be freely chosen, provided it is within the range of values for the three HBMs) for forward-propagating modes and $\bar{\beta} - K_z$ for backward modes. Note that s_j has been replaced with $-s_i$ in (17) and (18), as required for non-zero field overlap. The coupled mode equations then take the form:

$$\begin{aligned} \dot{F}_1 &= i(\kappa_{1\bar{1}}B_{\bar{1}} + \kappa_{10}B_0 + \kappa_{11}B_1) + i\varphi_1 F_1 \\ \dot{F}_0 &= i(\kappa_{0\bar{1}}B_{\bar{1}} + \kappa_{00}B_0 + \kappa_{01}B_1) + i\varphi_0 F_0 \\ \dot{F}_{\bar{1}} &= i(\kappa_{\bar{1}\bar{1}}B_{\bar{1}} + \kappa_{\bar{1}0}B_0 + \kappa_{\bar{1}1}B_1) + i\varphi_{\bar{1}} F_{\bar{1}} \\ \dot{B}_1 &= -i(\kappa_{1\bar{1}}^* F_{\bar{1}} + \kappa_{10}^* F_0 + \kappa_{11}^* F_1) + i\vartheta_1 B_1 \\ \dot{B}_0 &= -i(\kappa_{0\bar{1}}^* F_{\bar{1}} + \kappa_{00}^* F_0 + \kappa_{01}^* F_1) + i\vartheta_0 B_0 \\ \dot{B}_{\bar{1}} &= -i(\kappa_{\bar{1}\bar{1}}^* F_{\bar{1}} + \kappa_{\bar{1}0}^* F_0 + \kappa_{\bar{1}1}^* F_1) + i\vartheta_{\bar{1}} B_{\bar{1}} \end{aligned} \tag{19}$$

where

$$\varphi_q = \beta_q - \bar{\beta}, \vartheta_q = K_z - (\beta_q + \bar{\beta}) \tag{20}$$

are dephasing parameters that adjust the value of to match the propagation constants of each mode. Note again that all the coupling constants are (potentially) periodically modulated with spatial period $2\pi/3\alpha$.

That (19) conserves power can be proven by multiplying each equation by the conjugate of the amplitude in the derivative, and adding the resulting equations to their complex conjugate. After some manipulation and noting that:

$$n_a\kappa_{ab} = n_b\kappa_{ba} \tag{21}$$

we arrive at the final result:

$$\frac{d}{dz}\sum_i n_i(|F_i|^2 - |B_i|^2) = 0 \tag{22}$$

that is, $\sum_i n_i(|F_i|^2 - |B_i|^2) = \text{constant}$.

Once the scattering matrix has been found, it can be used to calculate the spectral response of the FBG for incidence of an arbitrary combination of forward-travelling modes.

REFERENCES

[1] W. Löffler, T. G. Euser, E. R. Eliel, M. Scharrer, P. St. J. Russell, and J. P. Woerdman, "Fiber transport of spatially entangled photons," *Physical Rev. Lett.*, vol. 106, no. 24, Jun. 2011, Art. no. 240505.

[2] A. E. Willner *et al.*, "Optical communications using orbital angular momentum beams," *Advances Opt. Photon.*, vol. 7, no. 1, pp. 66–106, Mar. 2015.

[3] N. Bozinovic *et al.*, "Terabit-scale orbital angular momentum mode division multiplexing in fibers," *Science*, vol. 340, no. 6140, pp. 1545–1548, 2013.

[4] P. Roth *et al.*, "Strong circular dichroism for the HE_{11} mode in twisted single-ring hollow-core photonic crystal fiber," *Optica*, vol. 5, no. 10, pp. 1315–1321, Oct. 2018.
[5] X. M. Xi *et al.*, "Optical activity in twisted solid-core photonic crystal fibers," *Physical Rev. Lett.*, vol. 110, no. 14, Apr. 2013, Art. no. 143903.
[6] R. Beravat, G. K. L. Wong, X. M. Xi, M. H. Frosz, and P. St. J. Russell, "Current sensing using circularly birefringent twisted solid-core photonic crystal fiber," *Opt. Lett.*, vol. 41, no. 7, pp. 1672–1675, Apr. 2016.
[7] R. P. Sopalla *et al.*, "Generation of broadband circularly polarized supercontinuum light in twisted photonic crystal fibers," *Opt. Lett.*, vol. 44, no. 16, pp. 3964–3967, Aug. 2019.
[8] R. Beravat, G. K. L. Wong, M. H. Frosz, X. M. Xi, and P. St. J. Russell, "Twist-induced guidance in coreless photonic crystal fiber: A helical channel for light," *Science Advances*, vol. 2, no. 11, 2016, Art. no. e1601421.
[9] P. Roth, G. K. L. Wong, M. H. Frosz, G. Ahmed, and P. St. J. Russell, "Full-field characterization of helical Bloch modes guided in twisted coreless photonic crystal fiber," *Opt. Lett.*, vol. 44, no. 20, pp. 5049–5052, Oct. 2019.
[10] S. Loranger *et al.*, "Bragg reflection and conversion between helical Bloch modes in twisted three-core optical fiber," in *Proc. Frontiers Opt. + Laser Sci. APS/DLS, Opt. Soc. America*, Washington, DC, USA, 2019, Paper FW1F.2.
[11] J. Li, G. Chen, P. Ma, L.-P. Sun, C. Wu, and B.-O. Guan, "Sampled Bragg gratings formed in helically twisted fibers and their potential application for the simultaneous measurement of mechanical torsion and temperature," *Opt. Express*, vol. 26, no. 10, pp. 12903–12911, May 2018.
[12] Y. Lu, C. Shen, D. Chen, J. Chu, Q. Wang, and X. Dong, "Highly sensitive twist sensor based on tilted fiber Bragg grating of polarization-dependent properties," *Opt. Fiber Technol.*, vol. 20, no. 5, pp. 491–494, Oct. 2014.
[13] L. Wang, P. Vaity, B. Ung, Y. Messaddeq, L. A. Rusch, and S. LaRochelle, "Characterization of OAM fibers using fiber Bragg gratings," *Opt. Express*, vol. 22, no. 13, pp. 15653–15661, Jun. 2014.
[14] X. M. Xi *et al.*, "Orbital-angular-momentum-preserving helical Bloch modes in twisted photonic crystal fiber," *Optica*, vol. 1, no. 3, pp. 165–169, Sep. 2014.
[15] P. St. J. Russell, R. Beravat, and G. K. L. Wong, "Helically twisted photonic crystal fibres," *Philosophical Trans. Roy. Soc. A: Math., Physical Eng. Sci.*, vol. 375, no. 2087, 2017, Art. no. 20150440.
[16] H. Kogelnik, "Coupled wave theory for thick hologram gratings," in *Proc. Landmark Papers Photorefractive Nonlinear Opt.: WORLD SCIENTIFIC*, 1995, pp. 133–171.
[17] P. St. J. Russell, "Bragg resonance of light in optical superlattices," *Physical Rev. Let.*, vol. 56, no. 6, pp. 596–599, Oct. 1986.
[18] R. Kashyap, *Fiber Bragg Gratings*, (Second Edition). Boston, MA, USA: Academic Press, 2010.
[19] Y. Wang, J. Grant, A. Sharma, and G. Myers, "Modified talbot interferometer for fabrication of fiber-optic grating filter over a wide range of bragg wavelength and bandwidth using a single phase mask," *J. Lightw. Technol.*, vol. 19, no. 10, pp. 1569–1573, Oct. 2001.
[20] M. Lorenzo *et al.*, "Spin-to-orbital conversion of the angular momentum of light and its classical and quantum applications," *J. Opt.*, vol. 13, no. 6, 2011, Art. no. 064001.
[21] B. J. Soller, D. K. Gifford, M. S. Wolfe, and M. E. Froggatt, "High resolution optical frequency domain reflectometry for characterization of components and assemblies," *Opt. Express*, vol. 13, no. 2, pp. 666–674, Jan. 2005.

Sébastien Loranger received the Ph.D. degree in engineering physics from Polytechnique Montreal, Montreal, QC, Canada, in 2018. He is currently working with photonic crystal fibers, Max-Planck Institute for the Science of Light in Erlangen, Germany, as a Postdoctoral Researcher. His research interest includes fiber Bragg gratings, fiber devices, photonic crystal fibers, and non-linear optics in gas and fibers.

Yang Chen received the Ph.D. degree in physics from Heriot-Watt University, Edinburgh, U.K. At the moment, he is working as a Postdoctoral Researcher with the Max Planck Institute for the Science of Light in Erlangen, Germany. His research interests include photonic-crystal-fiber optics, particularly on helically twisted fibers, low-loss antiresonant fibers, and transmission of orbital angular momentum in optical fibers.

Paul Roth received the master's degree in physics from the Friedrich Alexander University, Erlangen, Germany, in 2017. He is currently working toward the Ph.D. degree on photonic crystal fibers with the Max Planck Institute for the Science of Light in Erlangen, Germany. His research interests include photonic crystal fibers and non-linear fiber optics.

Michael H. Frosz received the Ph.D. degree in applied physics from the Technical University of Denmark, Kongens Lyngby, Denmark, in 2006 on theory and modeling of supercontinuum generation in photonic crystal fibers (PCFs). Since 2011, he has been the Head of the fabrication of PCFs with the Max Planck Institute for the Science of Light in Erlangen, Germany. His research interests includes all types of PCFs and their applications.

Gordon K. L. Wong received the M.Sc. and Ph.D. degrees from the University of Auckland, Auckland, New Zealand, in 2003 and 2008, respectively. He is currently working with the Max Planck Institute for the Science of Light in Erlangen, Germany. His research interests cover photonic crystal fibers and nonlinear fiber optics.

Philip St. J. Russell received the D.Phil. degree from the University of Oxford, Oxford, U.K., in 1979. He is a founding Director with the Max-Planck Institute for the Science of Light (MPL) and holds the Krupp Chair of Experimental Physics with the University of Erlangen-Nuremberg, Germany. His interests currently focus on scientific and technical applications of photonic crystal fibers. He is a Fellow of the Royal Society and the Optical Society (OSA) and has won a number of awards including the 2000 OSA Joseph Fraunhofer Award/Robert M. Burley Prize, the 2005 Thomas Young Prize of IOP, the 2005 Körber Prize for European Science, the 2013 EPS Prize for Research into the Science of Light, the 2014 Berthold Leibinger Zukunftspreis, the 2015 IEEE Photonics Award, and the 2018 Rank Prize for Optoelectronics. He was OSA's President in 2015, the International Year of Light.